Hydrodynamic characterization within a spinner flask and a rotary wall vessel for stem cell culture

Masoud Ghasemian,^a Carys Layton,^a Daniel Nampe,^{a,b} Nicole Isolde zur Nieden,^{b,c,d} Hideaki Tsutsui,^{a,b,d}* Marko Princevac^a

^aDepartment of Mechanical Engineering, University of California, Riverside, CA 92521

^bDepartment of Bioengineering, University of California, Riverside, CA 92521

^cDepartment of Molecular, Cell and Systems Biology, University of California, Riverside, CA 92521

^dStem Cell Center, University of California, Riverside, CA 92521

*Corresponding author: Hideaki Tsutsui, Ph.D., Email: htsutsui@engr.ucr.edu

Abstract

Stirred suspension culture is becoming a popular method for expanding human pluripotent stem cells (hPSCs). While stirring generates adequate fluid motions to lift the cells and facilitates mass transfers (of nutrients, dissolved gases, and metabolic wastes), excessive stirring could impose hydrodynamic forces deleterious for the growth of the cells. In this study, computational fluid dynamics (CFD) simulations were performed to first investigate hydrodynamic characteristics of fluid flows in a spinner flask, a common stirred suspension culture vessel used in laboratories. Flow patterns and distributions of shear stresses and the Kolmogorov length scales at varying impeller speeds were obtained. Comparison of the Kolmogorov length scales and sizes of hPSC aggregates, measured in the authors' previous experimental study, showed a strong correlation between the two. In addition to the spinner flask which generated complex and transient turbulent flows, this study investigated a newly developed rotary wall vessel that had been designed to produce laminar, circular Couette flows in order to control shear stress. CFD simulations revealed significantly more uniform and homogeneous flows compared to those in the

spinner flask, proposing a suitable culture vessel to investigate roles of shear stress on hPSCs in suspension.

Keywords: Pluripotent stem cell; Computational Fluid Dynamics; Spinner flask; Shear stress; Cell aggregate size; Stirred suspension culture

Nomenclature			
Symbols	1	μ_t	subgrid scale turbulent viscosity
C	Cmagaringly, constant	_	[kg.m ⁻¹ . s ⁻¹]
C_s	Smagorinsky constant	ho	fluid density [kg/m ³]
G	filter function	τ	shear stress [Pa]
P	static pressure [Pa]	$ au^{SGS}$	subgrid scale stress [Pa]
Re	Reynolds number	Ω	impeller speed [rpm]
S_{ij}	strain rate tensor [s ⁻¹]	Ω_i	inner wall speed [rpm]
t	time [s]	Ω_o	outer wall speed [rpm]
T	period of revolution [s]		
и	fluid velocity [m/s]	Abbrevio	ations
x	coordinate vector [m]	CFD	Computational Fluid Dynamics
		hESCs	human embryonic stem cells
Greek Symbols		hiPSCs	human induced pluripotent stem cells
δ_{ij}	Kronecker delta	hPSCs	human pluripotent stem cells
Δ	filter width	LES	Large Eddy Simulation
ε	turbulent dissipation rate [m ² /s ³]	RMS	root mean square
η	Kolmogorov length scale [m]	rpm	revolutions per minute
μ	fluid dynamic viscosity [kg.m ⁻¹ . s ⁻¹]	SGS	subgrid-scale

1. **Introduction**

Human pluripotent stem cells (hPSCs), including human embryonic stem cells (hESCs) and induced pluripotent stem cells (hiPSCs), have the potential to transform the future of cell therapies thanks to their ability to expand indefinitely and differentiate into any cell type [1-3]. However, significant biological and engineering challenges remain to be addressed before stem cell mediated therapies can be routinely employed to treat patients in a safe and economical manner. For example, engineering a scalable culture system that can promote maintenance of

pluripotency and effective differentiation uniformly in a controllable manner is necessary to meet the anticipated clinical demands for hPSCs and their derivatives [4, 5].

hPSCs are routinely cultured as two-dimensional (2D), adherent monolayers in tissue culture dishes and flasks. However, this mode of culture is labor intensive and costly in reagents and materials. In addition, manual handling of the culture is susceptible to human errors, contamination, and batch-to-batch variations in both cell quality and quantity. These limitations have encouraged laboratories to investigate alternative modes of stem cell culture that are expected to be more amenable to scale up and automation [6-8].

A promising alternative to monolayer culture for hPSC expansion is suspension culture [5, 9-14]. Multiple accounts have demonstrated that undifferentiated hPSCs can be expanded in stirred suspension culture [6, 15-17]. Expansion using such a platform, however, has multiple challenges such as variations of microenvironmental conditions within the culture volume and unclear links between culture parameters and stem cell fate [17]. In particular, spinner flasks, a common stirred suspension culture system, have large temporal and spatial distributions of shear stress, which can promote heterogenous cell aggregate formation and apply nonhomogeneous forces that may promote spontaneous differentiation and compromise pluripotency [12]. There is also the risk of damaging cells from too high of shear stresses and turbulent eddies [13, 18].

Current stirred suspension culture systems are empirically optimized for application-specific purposes without knowing the entire effect of physical forces on the cells. hPSCs can sense and respond to biophysical cues in their microenvironments [19, 20]. However, the molecular mechanisms by which cells engage in mechanotransduction are not fully understood. Understanding how fluid shear stresses and other physical forces affect stem cell behavior such as protein expression and folding, contractile activity, proliferation, maintenance of pluripotency or differentiation would enable new designs of scalable stem cell culture systems that utilize fluid shear as a key input parameter. With such an ambitious goal, we recently reported our initial experimental study where we investigated effects of varying impeller speeds on undifferentiated hPSCs using Corning ProCulture spinner flasks [21]. Interestingly, varying impeller speeds (0, 40, 60, 80, and 100 rpm) resulted in significant differences in stem cell aggregate size, population growth, maintenance of pluripotency, spontaneous differentiation, and protein kinase expressions.

The primary objective of the current study is to characterize the complex fluid flows within the spinner flask by reproducing the experimental conditions (e.g., culture volume and impeller speeds) using powerful Computational Fluid Dynamics (CFD) simulations. CFD simulations have been previously employed to understand the hydrodynamic characteristics within bioreactors [13, 14, 22-24]. In particular, researchers from CSIRO Australia have successfully employed Large Eddy Simulation (LES) to study the flow field within stirred suspension culture systems, including the Corning ProCulture spinner flask, and experimentally validated the simulation results using particle image velocimetry (PIV) [13, 14]. Here we take a similar LES approach to simulate complex flow fields corresponding to our previous report [21] and compute key flow properties such as shear stress and the Kolmogorov length scale [25, 26]. We compared the distribution of the Kolmogorov length scale to that of stem cell aggregate size which we measured in our previous study [21]. Finally, we performed CFD simulations of a newly developed custom rotary wall vessel, which features a pair of concentric rotating cylindrical walls designed to produce a laminar, circular Couette flow, resulting in a narrow and controlled distribution of shear stress.

2. Methods

This paper studied the hydrodynamics characteristics inside two different stem cell culture vessels. The first culture vessel chosen for this study was a Corning ProCulture spinner flask featuring a magnet-driven impeller and three baffles located on the vessel to promote mixing (Fig. 1). Although the standard working volume of this spinner flask is 125 mL, a 50 mL working volume was used to be consistent with our previous experimental study [21]. The second culture vessel was a rotary wall vessel designed to impose more uniform shear stress on the stem cells (Fig. 2). The inner radius, the outer radius, and the length are 30 mm, 37.5 mm and 94 mm, respectively, resulting in a working volume of 150 mL (Fig. 2). The commercial CFD solver, ANSYS CFX Version 18 (ANSYS Inc., Canonsburg, Pennsylvania, USA), was employed to solve governing equations (section 2.3). The fluid inside both devices is considered Newtonian and incompressible.

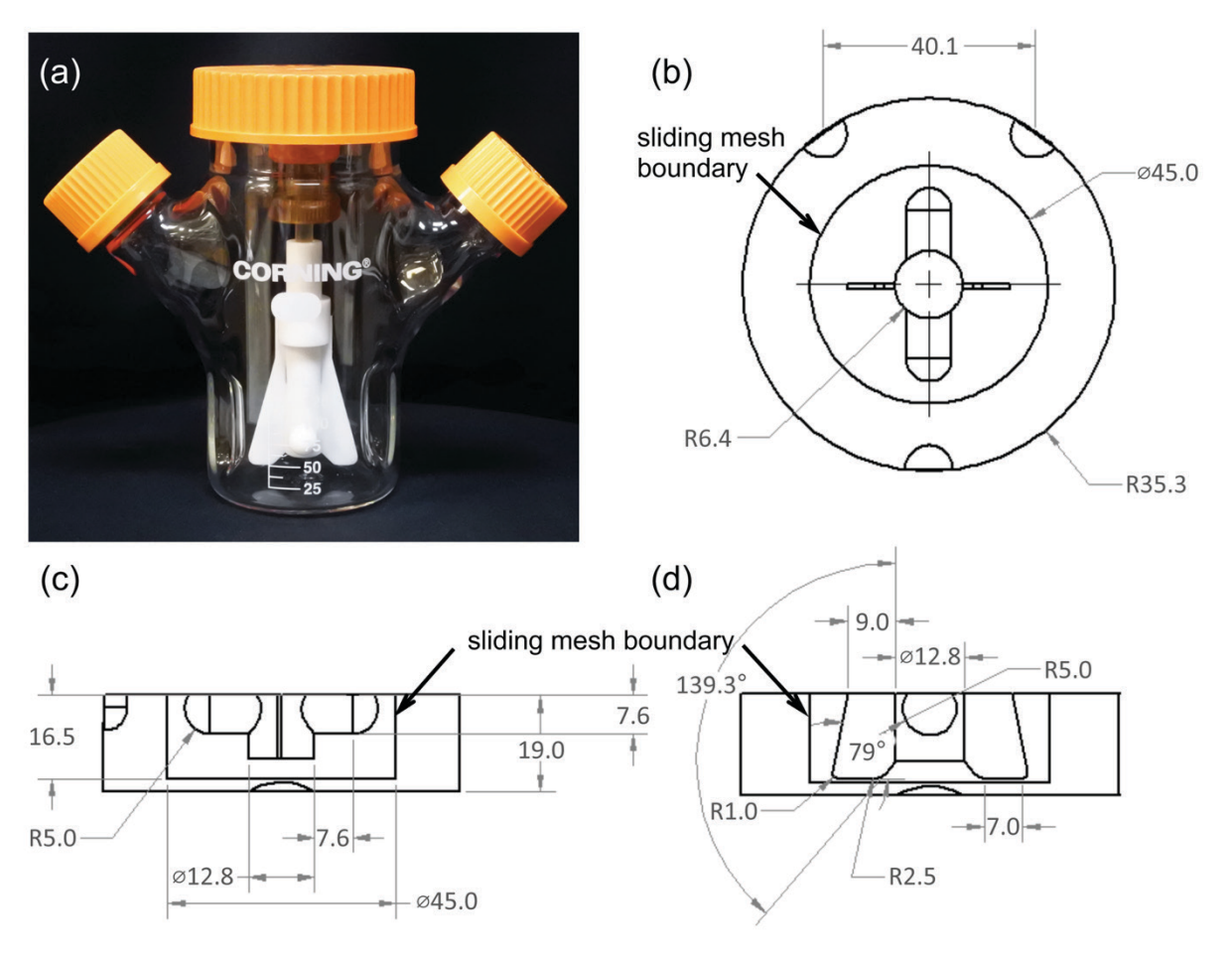


Figure 1: Spinner flask. (a) Corning ProCulture spinner flask. (b, c, d) Horizontal and vertical cross-sections of the computational domain used in this study. Measurements are in mm, unless otherwise noted.

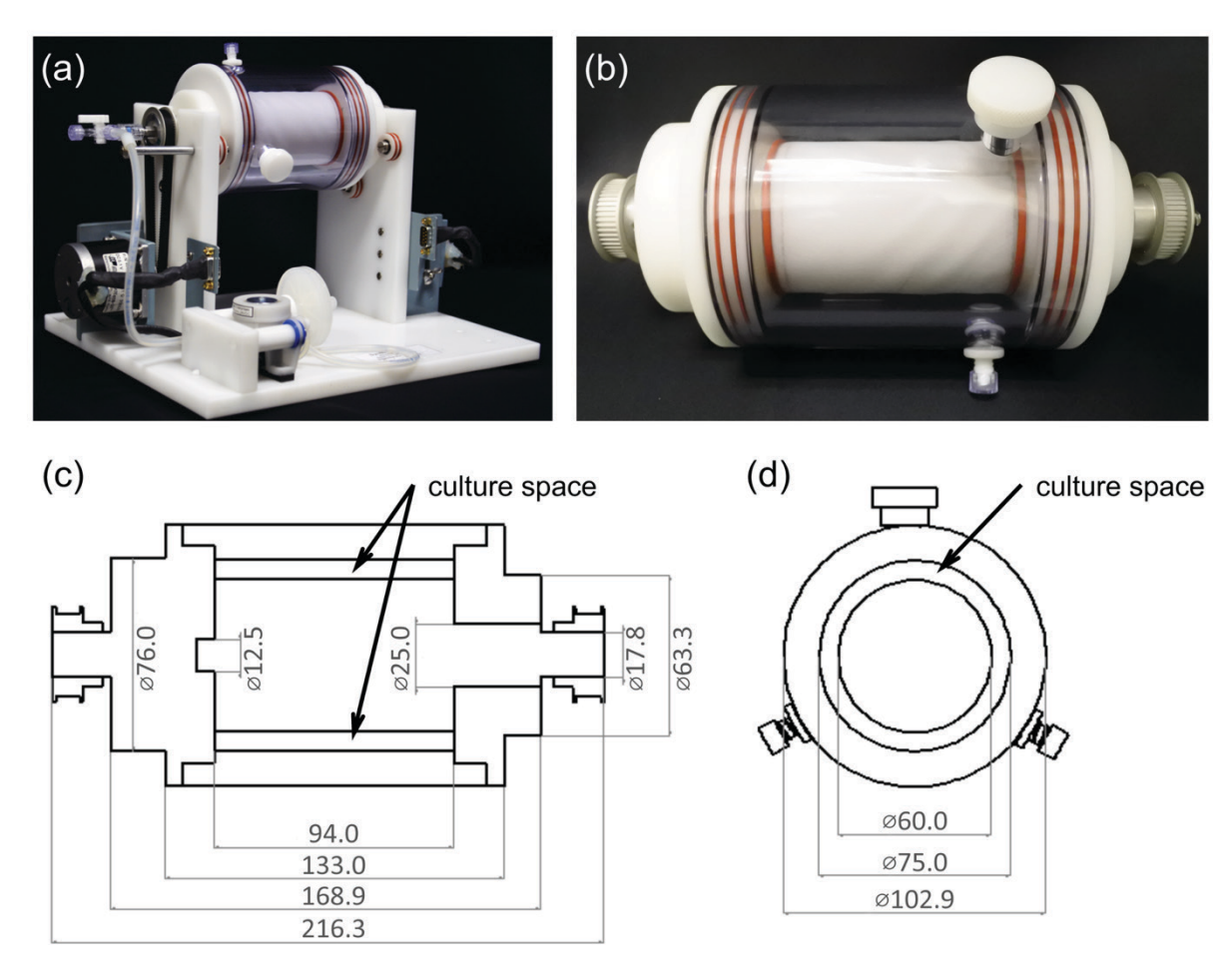


Figure 2: Rotary wall vessel. (a) The entire platform of the rotary wall vessel culture system. (b) Close view of the cylindrical vessel. (c, d) Cross sections of the vessel. Measurements are in mm.

2.1 Spinner flask

An unstructured grid was generated using ANSYS Meshing. The computational grid included 3.2 million elements (Fig. 3a). The computational domain was divided into a rotating region close to the impeller which was surrounded by a stationary region. Inflation layers were used close to the walls and impeller to capture the boundary layer. The interaction between the rotating and stationary regions was accounted for by using a transient rotor-stator technique (also known as a sliding mesh technique). The simulation was carried out for impeller speeds of 40, 60, 80, and 100 rpm. Due to the complex geometry of the impeller and the baffles, the flows for these rotational speeds were considered turbulent. Therefore, LES was employed to capture the turbulent field. A high-resolution scheme, the second-order backward Euler scheme, and a second-order upwind scheme were used for the advection term, the temporal terms, and turbulence modeling, respectively. The Gauss's divergence theorem and finite-element shape functions were utilized to

evaluate the control volume gradients. The residual target was that the normalized root mean square (RMS) errors for each conservation balance over the entire mesh fell to less than 10^{-5} . The time step was chosen in a way that the impeller rotated 1° each time step. LES was initialized with the results of steady-state k- ω (SST) turbulence modeling simulations. All simulations were run for ten revolutions, and only data for the last five revolutions were collected for the averaging process.

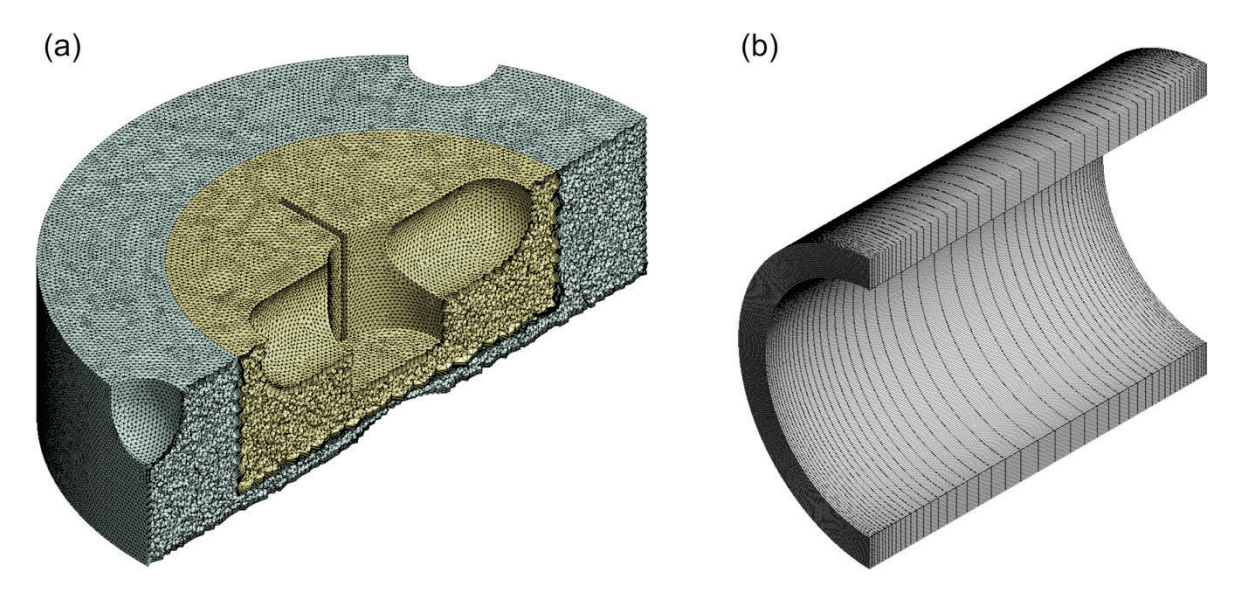


Figure 3: The computational grids for the spinner flask and the rotary wall vessel. (a) Unstructured grid used for the spinner flask, showing computational elements and inflation layers. Half of the entire domain (360°) is shown. (b) Structured grid used for the rotary wall vessel showing densely clustered elements near the walls. Half of the entire domain (full cylinder) is shown.

2.2 Rotary wall vessel

Due to the geometrical simplicity of the rotary wall vessel, a structured grid was generated using ANSYS Meshing. The computational grid included 425,000 hexahedral elements (Fig. 3b). Depending on the simulation case, the inner or outer wall rotated with a rotational speed of 40, 60, 80, or 100 rpm. Because of the Reynolds number (Re= $\rho R_o^2 \Omega_o/\mu \approx$ 6600 and 16500 for 40 rpm and 100rpm, respectively), the flow inside the rotary wall vessel was considered laminar [27]. The high-resolution scheme and the second-order backward Euler scheme were used for the advection term and the temporal terms, respectively. The Gauss's divergence theorem and finite-element shape functions were utilized to evaluate the control volume gradients. The residual target was that the normalized RMS errors for each conservation balance over the entire mesh fell to less than 10°

⁵. The time step was set to 0.01 s. The simulations were initialized with a zero value for all velocity components. All simulations were run for ten revolutions and only data for the last five revolutions were collected for the averaging process.

2.3 Governing equations

As mentioned earlier, LES was utilized to capture the turbulence field inside the spinner flask. The rationale behind LES is to separate the large scale and the small scale in the flow. The larger scale turbulent motions are solved directly, and the influence of smaller scales are taken into account by appropriate subgrid-scale (SGS) models [28]. The flow variables (velocity vector u_i and static pressure p) are decomposed into supergrid and subgrid scale components as follows:

$$u_i = \langle u \rangle_i + u_i' \tag{1}$$

$$p = \langle p \rangle + p' \tag{2}$$

To obtain the supergrid components, the following filtering operation is used [29]:

$$\langle u \rangle_i = \int_D G(\mathbf{x} - \mathbf{x}') \, u_i(\mathbf{x}') d\mathbf{x}' \tag{3}$$

$$\langle p \rangle = \int_{D} G(\mathbf{x} - \mathbf{x}') \, p(\mathbf{x}') d\mathbf{x}' \tag{4}$$

where integration is over the entire flow domain D, and the specified filter function, G, determines the scale of resolved eddies and satisfies the normalized condition [29]:

$$\int_{D} G(\mathbf{x} - \mathbf{x}') d\mathbf{x}' = 1 \tag{5}$$

The filtered governing equations for LES are obtained by filtering the continuity equation and the Navier-Stokes equations as follows [14, 29]:

$$\frac{\partial \langle u \rangle_j}{\partial x_j} = 0 \tag{6}$$

$$\rho\left(\frac{\partial\langle u\rangle_i}{\partial t} + \frac{\partial\langle u\rangle_i\langle u\rangle_j}{\partial x_j}\right) = -\frac{\partial\langle p\rangle}{\partial x_i} + \frac{\partial}{\partial x_j} \left[\mu\left(\frac{\partial\langle u\rangle_i}{\partial x_j} + \frac{\partial\langle u\rangle_j}{\partial x_i}\right)\right] - \frac{\partial\tau_{ij}^{SGS}}{\partial x_j}$$
(7)

where ρ is the fluid density, μ is the fluid dynamic viscosity, and τ_{ij}^{SGS} is the SGS stress tensor. τ_{ij}^{SGS} is modeled using the Boussinesq hypothesis as [30]

$$\tau_{ij}^{SGS} - \frac{1}{3} \delta_{ij} \tau_{kk} = -\mu_t \left(\frac{\partial \langle u \rangle_i}{\partial x_j} + \frac{\partial \langle u \rangle_j}{\partial x_i} \right) \tag{8}$$

where μ_t is the subgrid scale turbulent viscosity. The Smagorinsky kernel is used to obtain μ_t [31]:

$$\mu_t = \rho (C_s \Delta)^2 \sqrt{2 \langle S \rangle_{ij} \langle S \rangle_{ij}} \tag{9}$$

where C_s is the Smagorinsky constant and $C_s = 0.1$ was used in this study [29]. $\Delta = (\Delta x \Delta y \Delta z)^{1/3}$ is the filter width, and $\langle S \rangle_{ij}$ is the supergrid strain rate tensor defined as

$$\langle S \rangle_{ij} = \frac{1}{2} \left(\frac{\partial \langle u \rangle_i}{\partial x_j} + \frac{\partial \langle u \rangle_j}{\partial x_i} \right) \tag{10}$$

Previous studies have shown that the effects of hydrostatic pressure on cells are negligible compared to the effects of shear stress [32, 33]. Therefore, the current study focused on shear stress, which was calculated as follows [14, 29]:

$$\tau(\mathbf{x},t) = (\mu + \mu_t) \sqrt{\langle S \rangle_{ij} \langle S \rangle_{ij}} \tag{11}$$

As mentioned in Sections 2.1, all simulations were run for ten revolutions and the data from the last five revolutions were used for the averaging purpose. Accordingly, the time-averaged shear stress over the five revolution was computed as

$$\bar{\tau}(\mathbf{x}) = \frac{1}{5T} \int_{5T}^{10T} \tau(\mathbf{x}, t) dt = \frac{1}{5T} \int_{5T}^{10T} (\mu + \mu_t) \sqrt{\langle S \rangle_{ij} \langle S \rangle_{ij}}$$
(12)

where *T* is the period of one impeller revolution.

3. Results and discussion

3.1 Spinner flask

Figure 4 shows the magnitude of instantaneous velocity vector on a vertical plane through the center of spinner flask for an impeller speed of Ω =60 rpm. Several clockwise and counterclockwise vortices were observed inside the flask. However, the number and location of these eddies varied with time. As expected, the velocity had the maximum value at the tip of the impeller. The flow below the impeller, however, has a lower velocity than the surrounding regions. Cells can become trapped in this region and grow into large cell aggregates. The spinner flasks have an indentation in the center bottom specifically to prevent this stagnation.

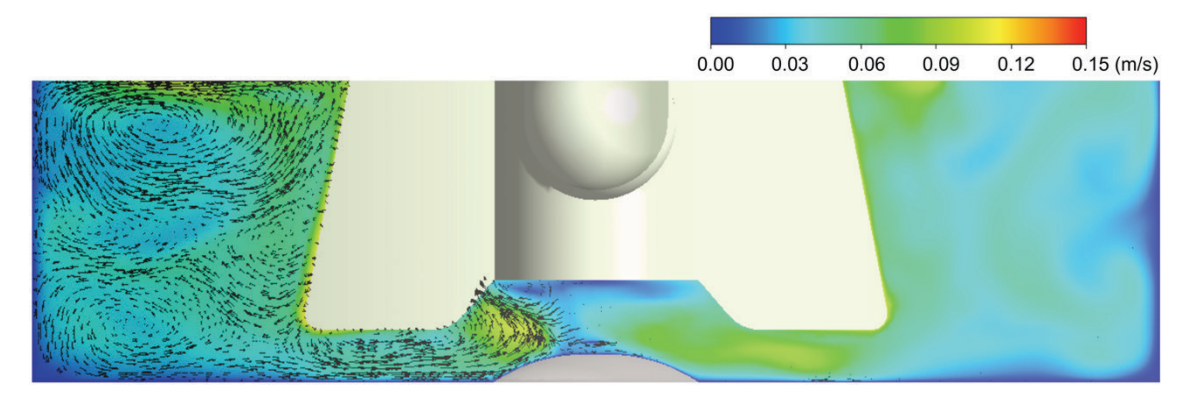


Figure 4: Contour of instantaneous velocity magnitude on a vertical plane through the center of spinner flask for an impeller speed of $\Omega = 60$ rpm. The left side includes the velocity vectors to show different eddies in the flow.

Figure 5 shows the corresponding instantaneous shear stress on a vertical plane through the center of spinner flask for an impeller speed of Ω =60 rpm. Regions of high shear stresses were observed close to the impeller tip and the bottom of the flask. In these regions, the shear stress exceeds 100 mPa. High shear stress and small eddies in these regions could damage cells [34].

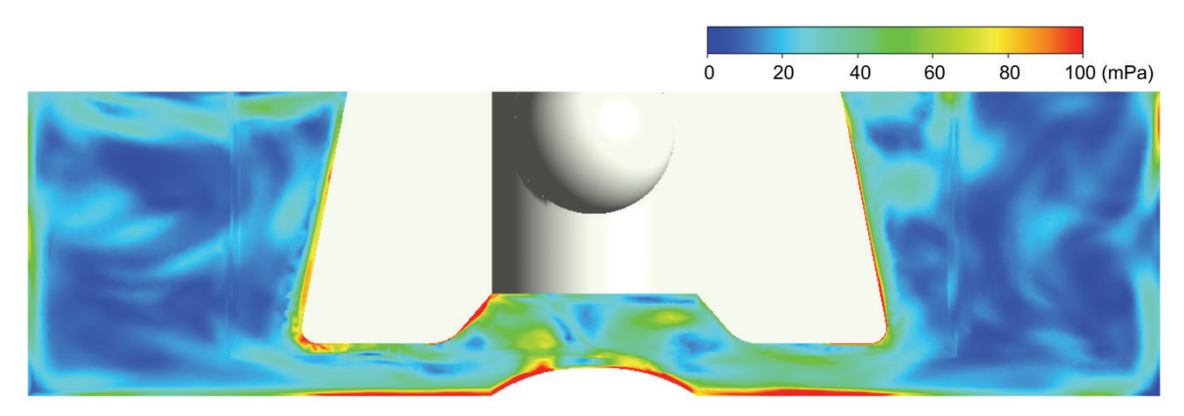


Figure 5: Contour of instantaneous shear stress on a vertical plane through the center of spinner flask for an impeller speed of $\Omega = 60$ rpm.

To get an overall picture of shear stress inside the spinner flask, the shear stress distributions across the computational domain averaged over 5 revolutions at different impeller speeds were plotted in Figure 6. As expected, increasing the impeller speeds moved the distribution towards higher shear stresses. For instance, at 40 rpm, the shear stress mostly varied between 5-20

mPa, while for 100 rpm it varied mainly from 15-100 mPa. To get better insight, data were analyzed, and different descriptive statistics parameters such as average, standard deviation, median, Q₁, and Q₃ were calculated (Fig. 7).

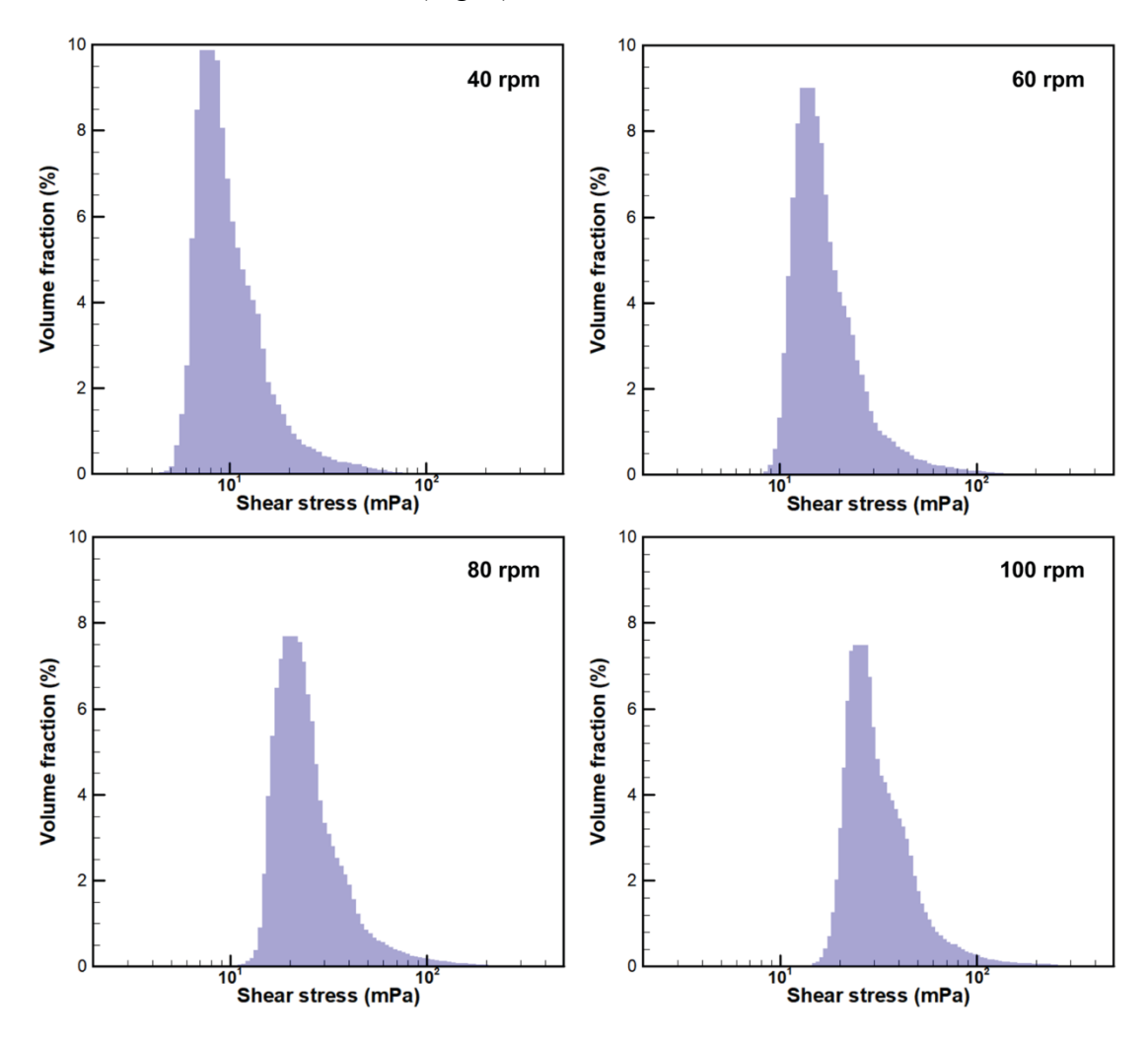


Figure 6: Distribution of time-averaged shear stresses within spinner flask for impeller speeds of $\Omega = 40,60,80$ and 100 rpm.

Figure 7 shows the boxplots for time-averaged shear stresses inside the spinner flask for impeller speeds of Ω =40, 60, 80 and 100 rpm. These boxplots were plotted using the *matplotlib* library in Python. For better visualization, outlier data were not included in the boxplots. The outliers were neglected by setting *showfliers* parameter as *False* [35]. The outliers were defined as the data outside [(Q₁ - 1.5 IQR), (Q₃ + 1.5 IQR)] range, where Q₁ and Q₃ are the first and third quartiles and IQR is Q₃ – Q₁. The median shear stress increased linearly with the impeller speed. For instance, increasing impeller speed from 40 rpm to 100 rpm raised the median of shear stress

from 11 mPa to 35 mPa. The mean shear stresses were 15, 25, 36 and 46 mPa for $\Omega = 40,60,80$ and 100 rpm, respectively. The standard deviations were 11, 19, 29, and 38 mPa for $\Omega = 40,60,80$ and 100 rpm, respectively.

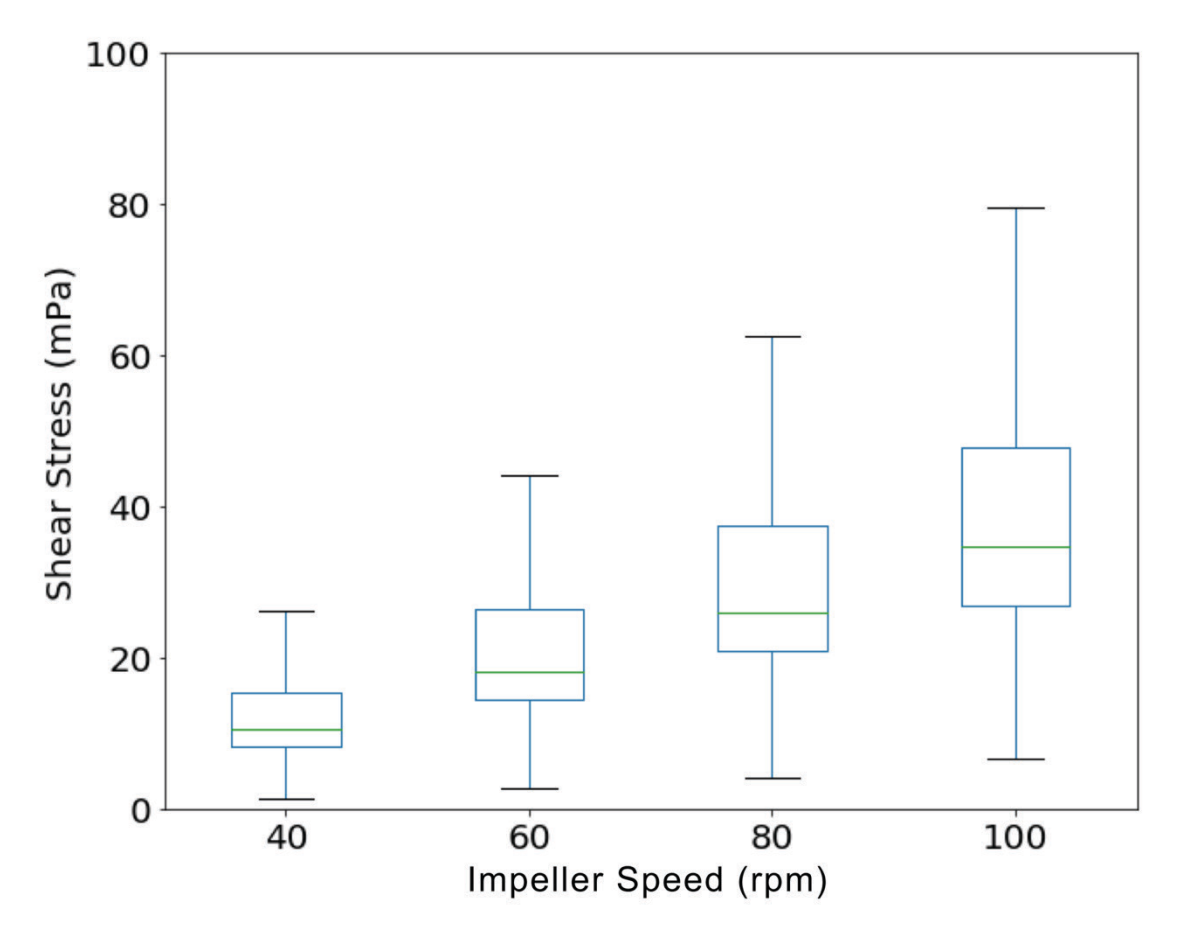


Figure 7: Boxplots of time-averaged shear stresses inside the spinner flask for impeller speeds of $\Omega = 40,60,80$ and 100 rpm.

The turbulent flow inside the spinner flask can be described using Kolmogorov's theory of isotropic turbulence, which suggests that the energy generated by impeller rotation is transmitted to the fluid by the generation of large eddies [36]. These large eddies split into smaller eddies due to inertial and friction forces. When the eddy size reaches a threshold (known as the Kolmogorov length scale), the viscous forces become predominant over the inertial forces [37]. The Kolmogorov length scale, η is proportional to $(\mu^3/\rho^3 \varepsilon)^{1/4}$, where ε is the turbulent dissipation rate [14]. In order to address the role of small scales of flow on cell growth, the Kolmogorov length scale was computed.

The distribution of Kolmogorov length scales inside the spinner flask is shown in Figure 8. Increases in impeller speeds shifted the Kolmogorov length scale distribution toward smaller values. This shift in distribution was due to higher dissipation rate at higher impeller speeds. The Kolmogorov length scale ranged from 100 μ m to ~400 μ m at 40 rpm while it ranged from 40 μ m to ~210 μ m for 100 rpm.

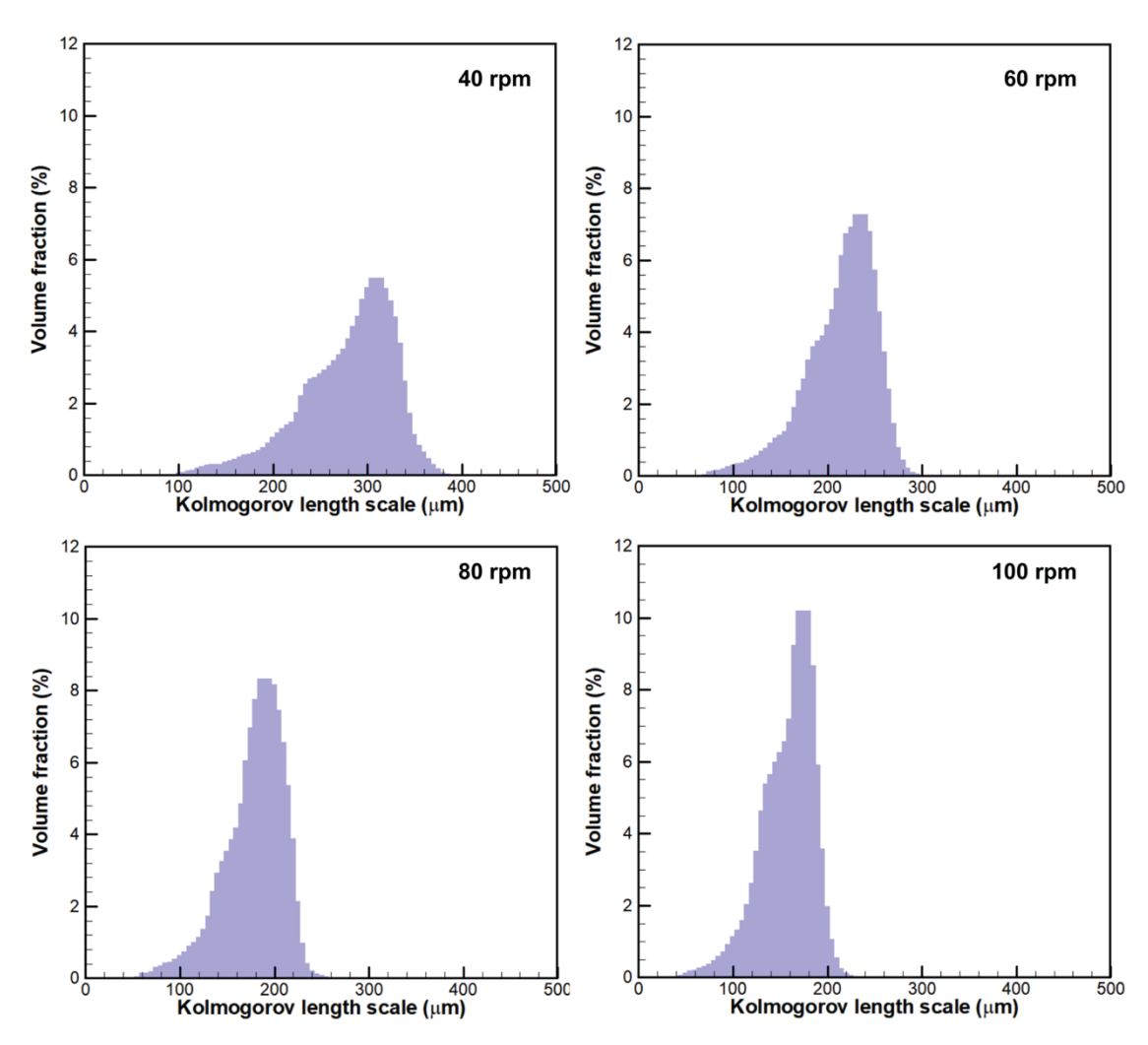


Figure 8: Distribution of time-averaged Kolmogorov length scale within spinner flask for impeller speeds of $\Omega = 40,60,80$ and 100 rpm.

The boxplots for the time-averaged Kolmogorov length scale inside the spinner flask for impeller speeds of Ω =40, 60, 80 and 100 rpm are shown in Figure 9. The Kolmogorov length scale decreased with impeller speed. For example, increasing impeller speed from 40 rpm to 100 rpm decreased the mean Kolmogorov length scale from 264 μ m to 149 μ m.

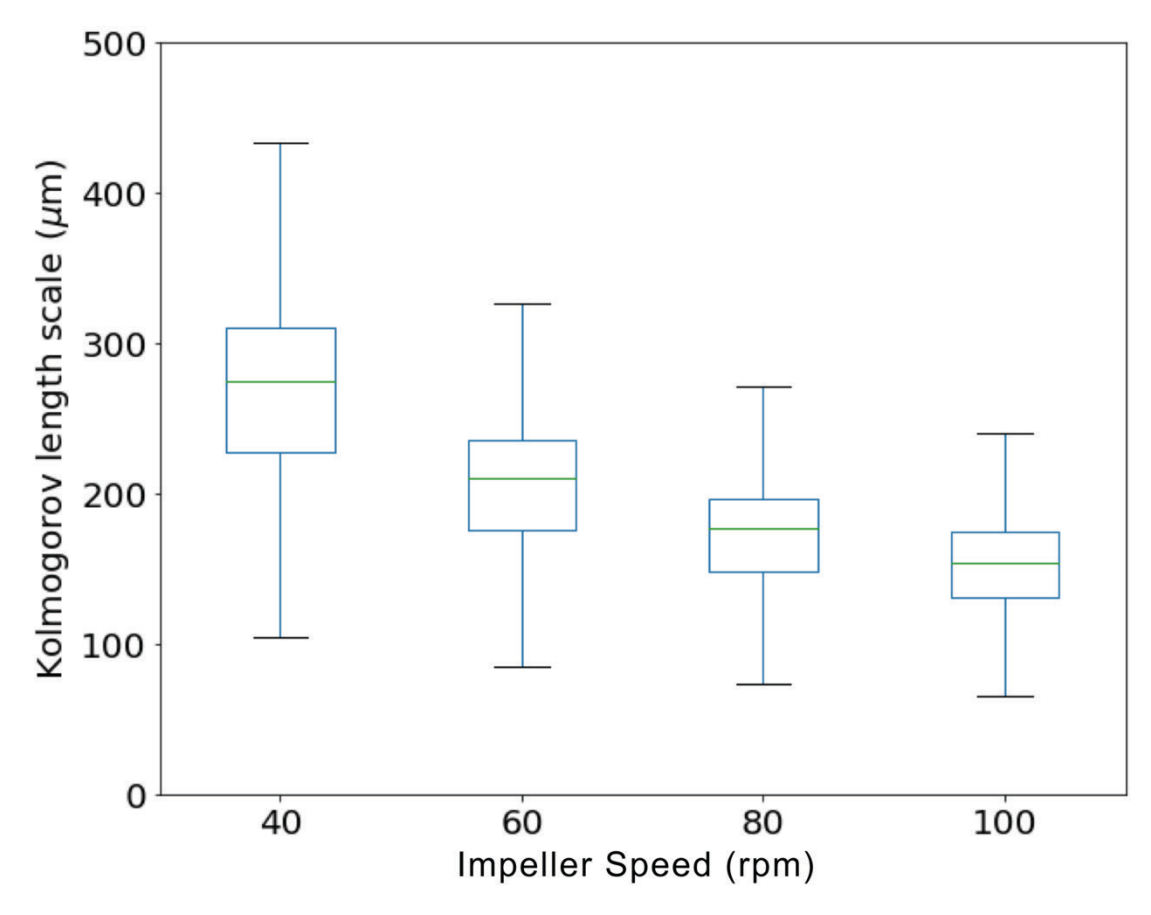


Figure 9: Boxplots of time-averaged Kolmogorov length scale inside the spinner flask for impeller speeds of $\Omega = 40,60,80$ and 100 rpm

The relationship between eddy size and cell aggregate size has been discussed in several studies [18, 34]. Sen et al. calculated the minimum Kolmogorov length scale based on the maximum energy dissipation rate near the tip of impeller [34]. However, the shear stress inside the spinner flask is not uniform. The current study calculated the volumetric distribution of Kolmogorov length scale rather than its maximum value.

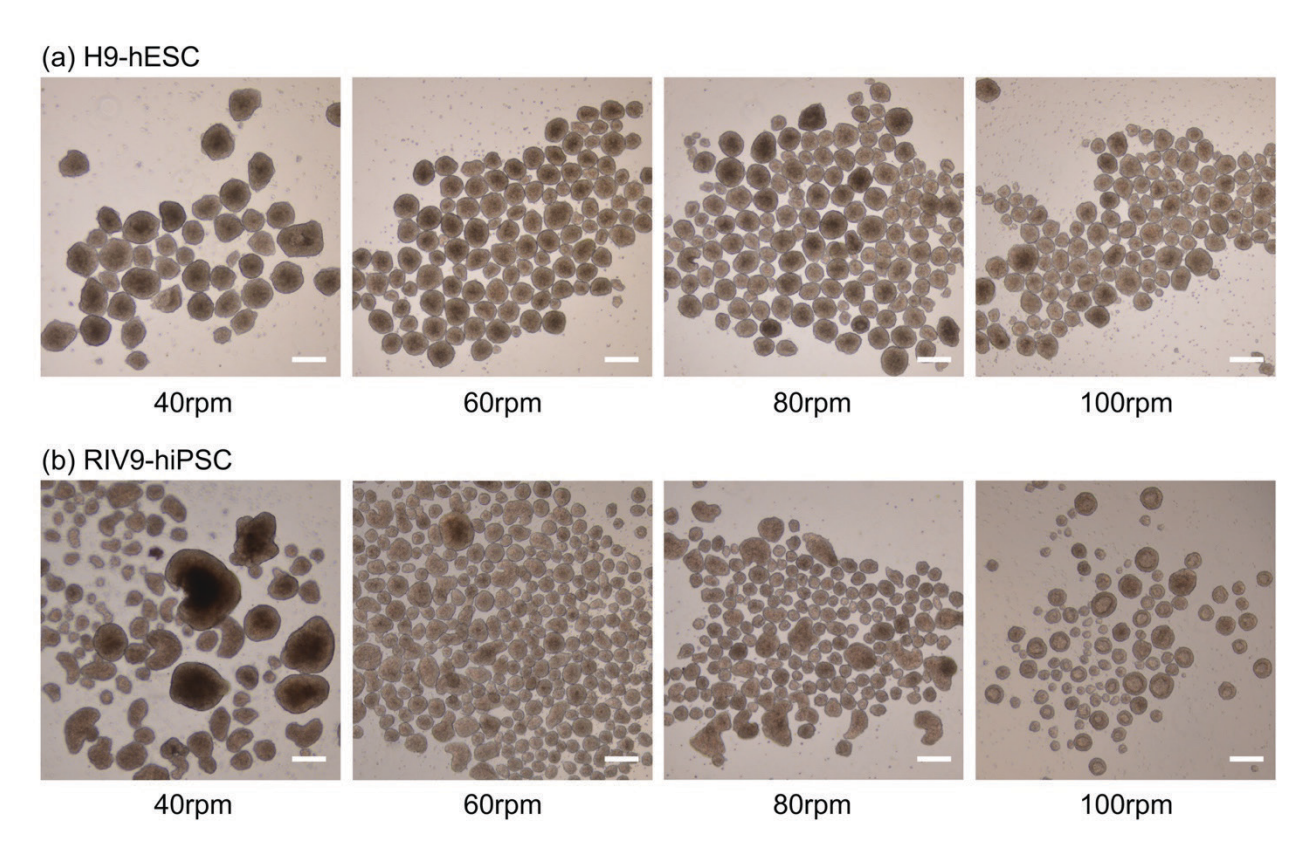


Figure 10: Photomicrographs of day 7 cell aggregates grown under different impeller speeds in spinner flasks. (a) H9 human embryonic stem cells. (b) RIV9 human induced pluripotent stem cells. Scale bars: $250 \mu m$.

Figure 10 shows photomicrographs of the day 7 aggregates of H9-hESCs and RIV9-hiPSCs at different impeller speeds in Corning ProCulture spinner flasks with a working volume of 50 mL [21]. These images show that the cell aggregate size decreased with increasing impeller speeds. Mean cell aggregate size for both H9-hESCs and RIV9-hiPSCs for different impeller speeds were compared with the Kolmogorov length scale in Figure 11. Smaller eddies led to smaller mean cell aggregate size. Also, the standard deviation was shown to indicate how wide the Kolmogorov length scale and cell aggregate size varied throughout the flask. At lower impeller speeds, the cell aggregates were larger due to lower shear stresses, but some of the aggregates might be broken up near the tip of the impeller. Hence, the 40-rpm condition had the largest standard deviation among the tested impeller speeds. Figure 11 also shows that the mean cell aggregate size for both H9-hESCs and RIV9-hiPSCs did not exceed the corresponding mean Kolmogorov length scale for any impeller speed. The distributions of the cell aggregate size reflect the trend observed in those of

the Kolmogorov length scale. Although further investigation is needed, it is possible that the Kolmogorov length scale controlled cell aggregate sizes.

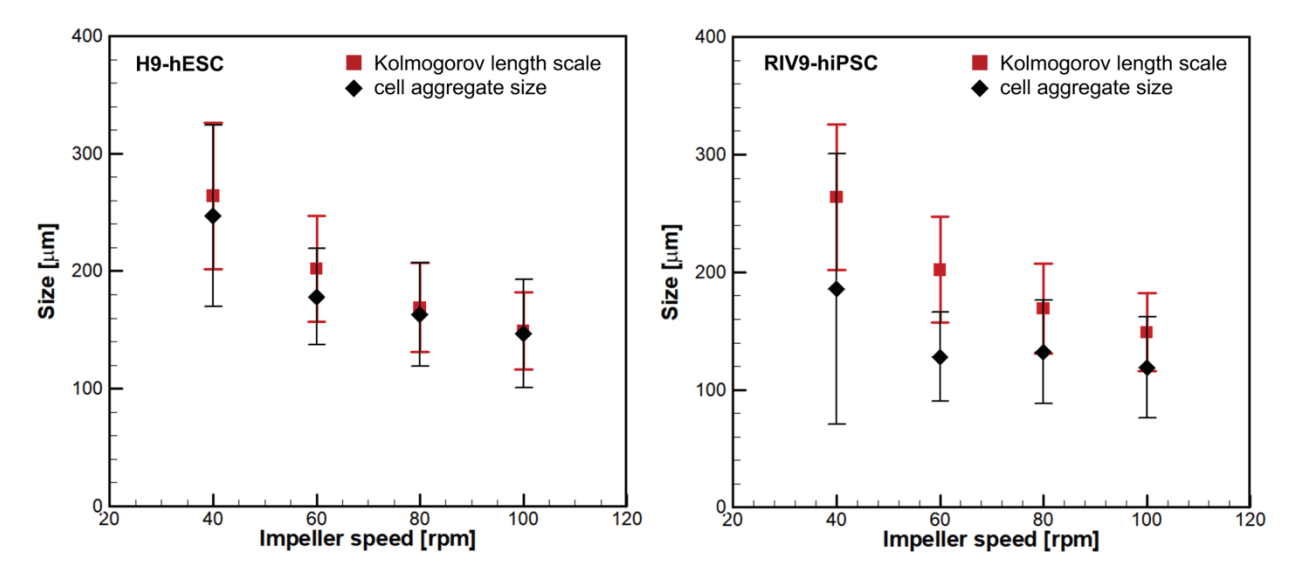


Figure 11: Comparison of cell aggregate size (black diamond) data [21] and the Kolmogorov length scale (red square) data from CFD simulation for different impeller speeds in spinner flask for H9-hESCs and RIV9-hiPSCs.

As stated before, the above CFD simulations were conducted using a working volume of 50 mL, corresponding to our previous experimental study [21]. Additional CFD results with the standard working volume of the Corning ProCulture spinner flask (125 mL) are provided in the supplementary information (Fig. S1 - S4).

3.2 Rotary wall vessel

As shown in section 3.1, the flow inside spinner flasks is transient and heterogeneous. Consequently, cells experience a wide range of shear stresses and Kolmogorov length scales. As discussed above, it is possible that the flow characteristics can impact cell expansion and differentiation. Therefore, having a uniform flow with homogeneous shear stress is expected to enhance the controllability and efficiency of both expansion and differentiation. In order to impose more uniform shear stress on stem cells, a rotary wall vessel that generates steady and reasonably uniform shear distribution was developed in collaboration with Synthecon, Inc. (Houston, TX) (Fig. 2).

Figure 12 shows the boxplots of time-averaged shear stresses within the rotary wall vessel for two scenarios. In the first scenario, the inner wall rotated with a rotational speed of 60 rpm and the outer wall and sidewalls were stationary (Ω_i =60 rpm, Ω_o = 0 rpm). In the second scenario, the outer wall and the sidewalls rotated at 60 rpm and the inner wall was kept stationary (Ω_i =0 rpm, Ω_o = 60 rpm). The mean shear stresses for both cases were about 28 mPa, while the standard deviation was significantly different. Rotating the inner wall led to a wider range of variation in the shear stress. For instance, the standard deviation for the first scenario (Ω_i =60 rpm, Ω_o = 0 rpm) was 29 mPa, while this value for second scenario (Ω_i =0 rpm, Ω_o = 60 rpm) was just 9 mPa.

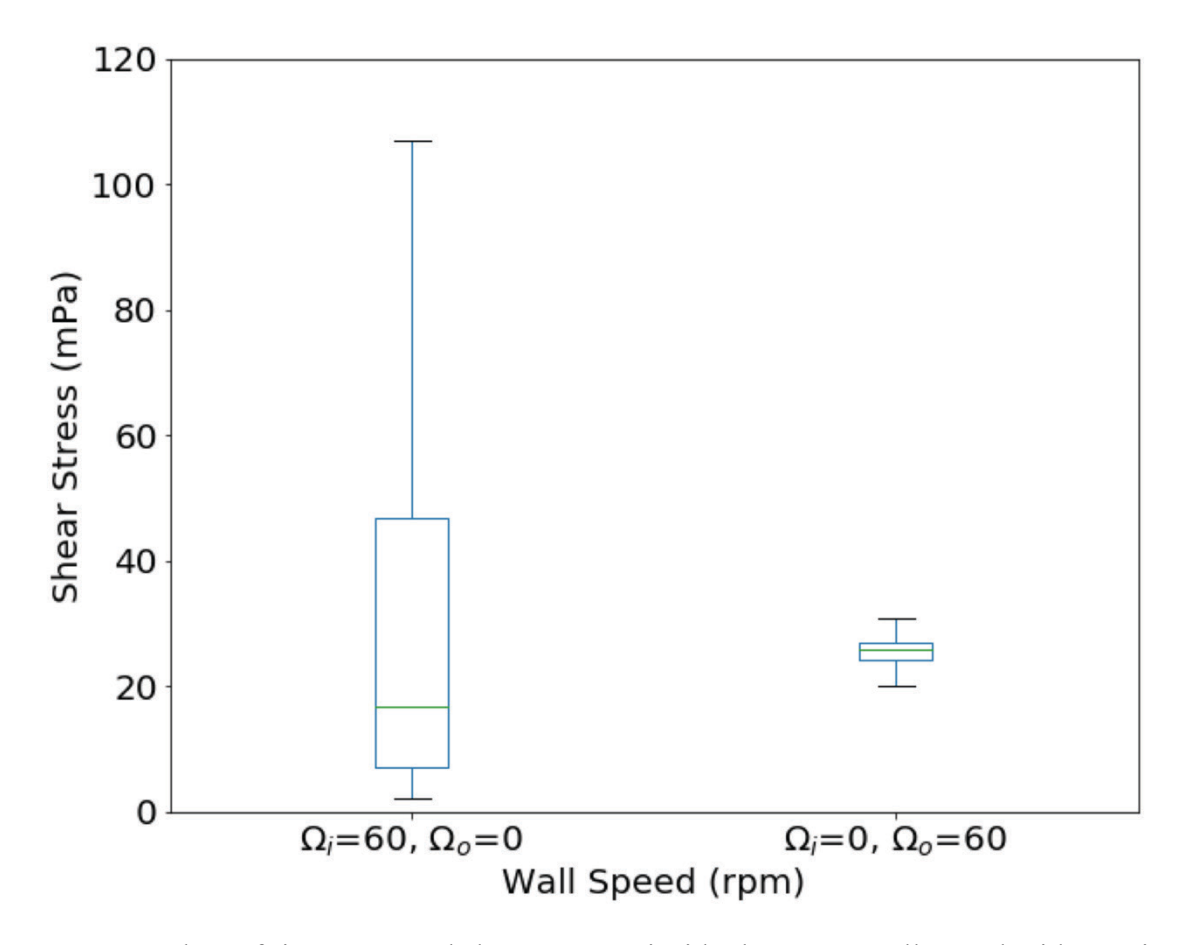


Figure 12: Boxplots of time-averaged shear stresses inside the rotary wall vessel with rotation of the inner or outer wall

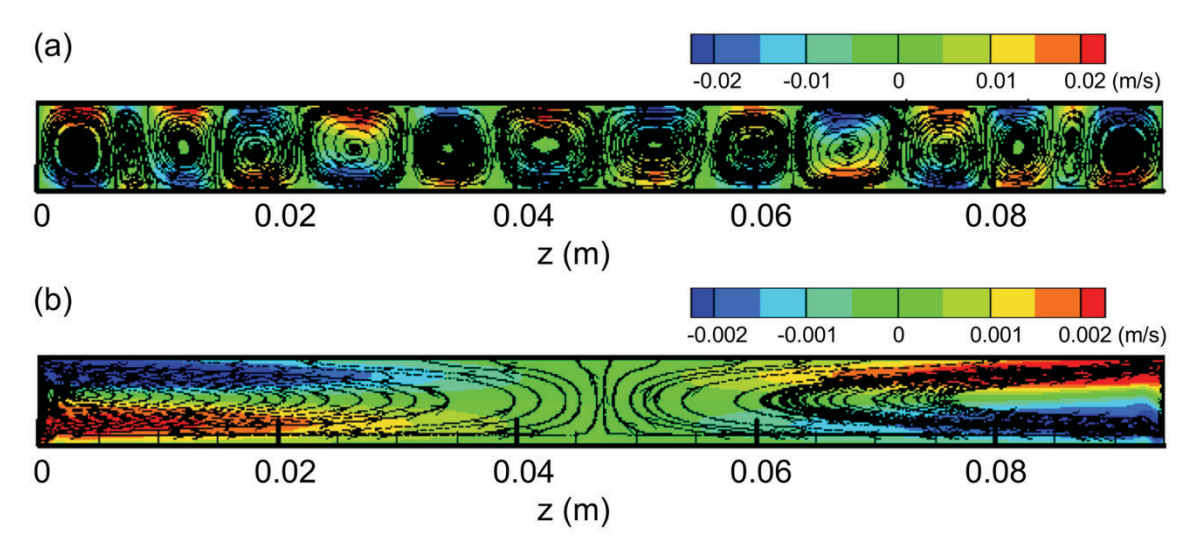


Figure 13: Streamlines and contour of instantaneous axial velocity within the space between the inner and outer walls. (a) The inner wall rotated at Ω_i =60 rpm, and the outer wall was stationary (Ω_o = 0 rpm). (b) The inner wall was stationary (Ω_i = 0 rpm), and the outer wall rotated at Ω_o =60 rpm.

In order to answer why the shear stress was remarkably different and understand the flow pattern differences between the two cases, the streamlines and contour of instantaneous axial velocity in the gap between the two cylinders were plotted in Figure 13. In the first scenario (Fig. 13a), there were numerous regions of low and high axial velocity, with its value reaching 20 mm/s, while in the second scenario (Fig. 13b), the regions of low and high axial velocity formed near the sidewalls, with its value reaching only 2 mm/s. This major difference in the flow pattern was due to the direction of centrifugal forces. In the first scenario, the centrifugal force was larger than the local pressure gradient. Therefore, the flow was unstable, and several Taylor vortices [38] were created inside the space, but in the second scenario, the centrifugal force was less than the local pressure gradient and the flow was stable. According to these results, rotating the outer wall leads to a more uniform and homogeneous flow. Therefore, it is easier to control the shear stress and consequently cell expansion and differentiation in this environment.

Due to the flow stability observed in the second scenario (Fig. 13b), we decided to keep the inner wall stationary and rotate the outer wall with different rotational speeds. Figures 14 and 15 show the histograms and the boxplots of shear stresses inside the rotary wall vessel for outer wall speeds of $\Omega_0 = 40,60,80$ and 100 rpm, respectively. The mean shear stresses were 19, 27,

36 and 44 mPa for $\Omega_0 = 40,60,80$ and 100 rpm, respectively. The standard deviation did not vary significantly with rotational speed.

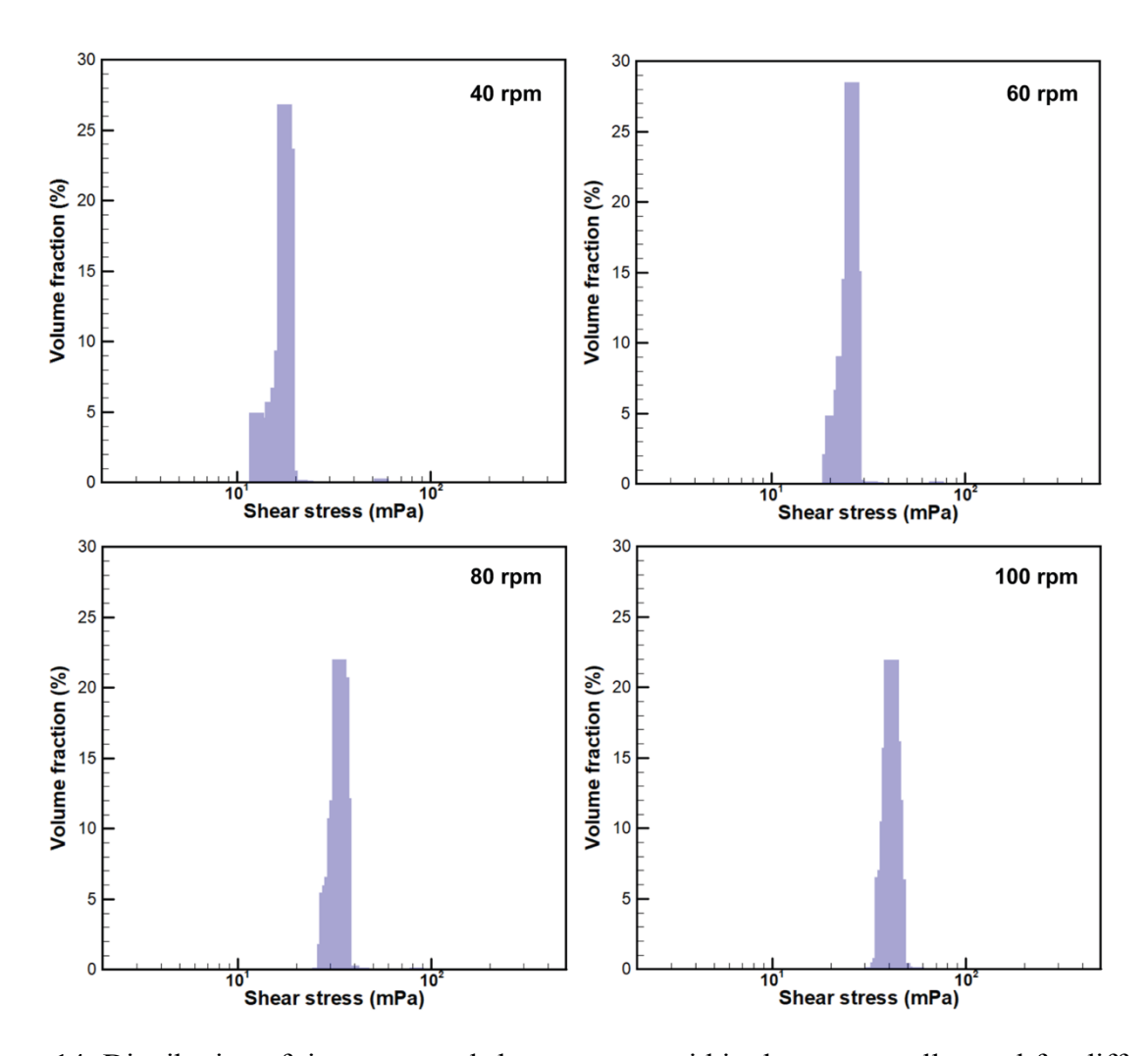


Figure 14: Distribution of time-averaged shear stresses within the rotary wall vessel for different outer wall speeds (Ω_0 =40, 60, 80 and 100 rpm) with a stationary inner wall.

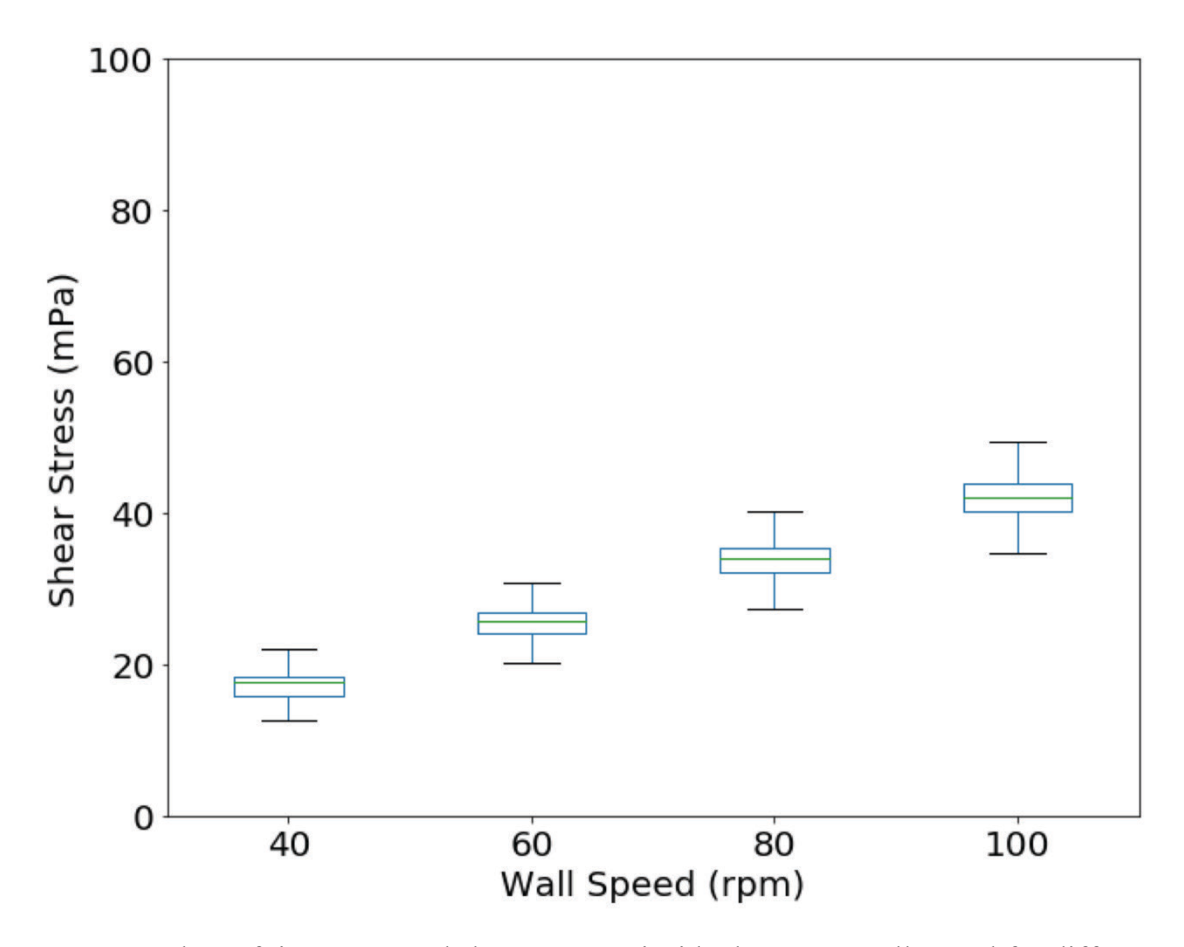


Figure 15: Boxplots of time-averaged shear stresses inside the rotary wall vessel for different outer wall speeds (Ω_0 =40, 60, 80 and 100 rpm).

Comparisons of shear stresses between the spinner flask (Fig. 6 and Fig. 7) and the rotary wall vessel (Fig. 14 and Fig. 15) showed that while the average shear stresses at certain rotating speeds were almost identical between the two vessels, the standard deviations were significantly different. For instance, the mean shear stresses at 60 rpm were around 26 mPa for both vessels but the standard deviation was 53% less in the rotary wall vessel compared to the spinner flask (9 mPa vs.19 mPa). Across the board, cell aggregates would experience a narrower range of shear stress in rotary wall vessel. Therefore, we believe the newly developed rotary wall vessel offers a better platform to investigate the roles of controlled mechanical forces, particularly shear stress, which is a key objective in our future study.

4. Conclusion

CFD simulations were carried out to characterize the hydrodynamics inside a spinner flask and a rotary wall vessel. The shear stress and Kolmogorov length scale distributions inside the cell culture vessels were examined for different operation speeds. The main conclusions are summarized as follows:

- Increasing the impeller speeds reduces the Kolmogorov length scale inside the spinner flask due to higher dissipation rates.
- The mean cell aggregate size for both H9-hESC and RIV9-hiPSC cells did not exceed the
 mean Kolmogorov length scale for any impeller speed. Although further investigation is
 needed, it is possible that the Kolmogorov length scale controls (not necessarily limit) the
 cell aggregate size.
- Rotating the inner cylinder creates Taylor vortices and secondary flow inside the rotary
 wall vessel which significantly increases the shear stress variations. This unwanted
 secondary flow can be minimized if the outer wall is rotated while the inner wall remains
 stationary.
- Cells would experience almost identical mean shear stresses inside both rotary wall vessel
 and spinner flask, but the shear stress variation could be much less in the rotary wall vessel
 compared to the spinner flask.

Acknowledgment

This work was supported by the National Science Foundation (Grant No. 1707190). Any opinion, findings, and conclusions or recommendations expressed in this material are those of the authors and do not necessarily reflect the views of the National Science Foundation. The authors acknowledge the High-Performance Computing Center at UC Riverside for its supercomputing resources made available for conducting the numerical simulations presented in this paper. The authors are also grateful for the support of ANSYS Inc. for providing the CFD software used for simulations carried out in this work.

References

- [1] J.A. Thomson, J. Itskovitz-Eldor, S.S. Shapiro, M.A. Waknitz, J.J. Swiergiel, V.S. Marshall, J.M. Jones, Embryonic stem cell lines derived from human blastocysts, science, 282 (1998) 1145-1147.
- [2] K. Takahashi, K. Tanabe, M. Ohnuki, M. Narita, T. Ichisaka, K. Tomoda, S. Yamanaka, Induction of pluripotent stem cells from adult human fibroblasts by defined factors, cell, 131 (2007) 861-872.
- [3] Kevin G. Chen, Barbara S. Mallon, Ronald D.G. McKay, Pamela G. Robey, Human Pluripotent Stem Cell Culture: Considerations for Maintenance, Expansion, and Therapeutics, Cell Stem Cell, 14 (2014) 13-26.
- [4] D. Jing, A. Parikh, J.M. Canty, E.S. Tzanakakis, Stem Cells for Heart Cell Therapies, Tissue Engineering Part B: Reviews, 14 (2008) 393-406.
- [5] M. Serra, C. Brito, C. Correia, P.M. Alves, Process engineering of human pluripotent stem cells for clinical application, Trends in Biotechnology, 30 (2012) 350-359.
- [6] M. Amit, J. Chebath, V. Margulets, I. Laevsky, Y. Miropolsky, K. Shariki, M. Peri, I. Blais, G. Slutsky, M. Revel, J. Itskovitz-Eldor, Suspension culture of undifferentiated human embryonic and induced pluripotent stem cells, Stem Cell Rev, 6 (2010).
- [7] S. Jung, K.M. Panchalingam, R.D. Wuerth, L. Rosenberg, L.A. Behie, Large-scale production of human mesenchymal stem cells for clinical applications, Biotechnology and Applied Biochemistry, 59 (2012) 106-120.
- [8] P. Ashok, Y. Fan, M.R. Rostami, E.S. Tzanakakis, Aggregate and Microcarrier Cultures of Human Pluripotent Stem Cells in Stirred-Suspension Systems, Methods in molecular biology (Clifton, N.J.), 1502 (2016) 35-52.
- [9] A.W. Nienow, Reactor Engineering in Large Scale Animal Cell Culture, Cytotechnology, 50 (2006) 9-33.
- [10] D. Schop, F.W. Janssen, E. Borgart, J.D. de Bruijn, R. van Dijkhuizen-Radersma, Expansion of mesenchymal stem cells using a microcarrier-based cultivation system: growth and metabolism, Journal of Tissue Engineering and Regenerative Medicine, 2 (2008) 126-135.
- [11] G. Eibes, F. dos Santos, P.Z. Andrade, J.S. Boura, M.M.A. Abecasis, C.L. da Silva, J.M.S. Cabral, Maximizing the ex vivo expansion of human mesenchymal stem cells using a microcarrier-based stirred culture system, Journal of Biotechnology, 146 (2010) 194-197.
- [12] K.M. Fridley, M.A. Kinney, T.C. McDevitt, Hydrodynamic modulation of pluripotent stem cells, Stem Cell Research & Therapy, 3 (2012) 45.
- [13] P. Liovic, I. Sutalo, R. Stewart, V. Glattauer, L. Meagher, Fluid flow and stresses on microcarriers in spinner flask bioreactors, Ninth International Conference on CFD in the Minerals and Process IndustriesMelbourne, Australia, 2012.
- [14] J.D. Berry, P. Liovic, I.D. Šutalo, R.L. Stewart, V. Glattauer, L. Meagher, Characterisation of stresses on microcarriers in a stirred bioreactor, Applied Mathematical Modelling, 40 (2016) 6787-6804.
- [15] H. Singh, P. Mok, T. Balakrishnan, S.N.B. Rahmat, R. Zweigerdt, Up-scaling single cell-inoculated suspension culture of human embryonic stem cells, Stem Cell Research, 4 (2010) 165-179.
- [16] R. Olmer, A. Lange, S. Selzer, C. Kasper, A. Haverich, U. Martin, R. Zweigerdt, Suspension Culture of Human Pluripotent Stem Cells in Controlled, Stirred Bioreactors, Tissue Engineering Part C: Methods, 18 (2012) 772-784.

- [17] R. Krawetz, J.T. Taiani, S. Liu, G. Meng, X. Li, M.S. Kallos, D.E. Rancourt, Large-scale expansion of pluripotent human embryonic stem cells in stirred-suspension bioreactors, Optimization, (2016).
- [18] M.S. Croughan, J.F. Hamel, D.I.C. Wang, Hydrodynamic Effects on Animal-Cells Grown in Microcarrier Cultures, Biotechnology and Bioengineering, 29 (1987) 130-141.
- [19] Y. Sun, C.S. Chen, J. Fu, Forcing stem cells to behave: a biophysical perspective of the cellular microenvironment, Annual review of biophysics, 41 (2012) 519-542.
- [20] D. Nampe, H. Tsutsui, Engineered micromechanical cues affecting human pluripotent stem cell regulations and fate, J Lab Autom, 18 (2013) 482-493.
- [21] D. Nampe, R. Joshi, K. Keller, I. zur Nieden Nicole, H. Tsutsui, Impact of fluidic agitation on human pluripotent stem cells in stirred suspension culture, Biotechnology and Bioengineering, 114 (2017) 2109-2120.
- [22] A. Amani, E. Jalilnejad, CFD modeling of formaldehyde biodegradation in an immobilized cell bioreactor with disc-shaped Kissiris support, Biochemical Engineering Journal, 122 (2017) 47-59.
- [23] B.S. Borys, E.L. Roberts, A. Le, M.S. Kallos, Scale-up of embryonic stem cell aggregate stirred suspension bioreactor culture enabled by computational fluid dynamics modeling, Biochemical Engineering Journal, 133 (2018) 157-167.
- [24] T.K. Villiger, B. Neunstoecklin, D.J. Karst, E. Lucas, M. Stettler, H. Broly, M. Morbidelli, M. Soos, Experimental and CFD physical characterization of animal cell bioreactors: From micro- to production scale, Biochemical Engineering Journal, 131 (2018) 84-94.
- [25] R.S. Cherry, E.T. Papoutsakis, Hydrodynamic effects on cells in agitated tissue culture reactors, Bioprocess Engineering, 1 (1986) 29-41.
- [26] R.S. Cherry, Animal cells in turbulent fluids: Details of the physical stimulus and the biological response, Biotechnology Advances, 11 (1993) 279-299.
- [27] D. Coles, Transition in Circular Couette Flow, Journal of Fluid Mechanics, 21 (1965) 385- &.
- [28] S.B. Pope, Turbulent Flows, Cambridge University Press, Campridge, United Kingdom, 2000.
- [29] ANSYS CFX-Solver Theory Guide Release 14.0, (2011).
- [30] J.O. Hinze, Turbulence, McGraw-Hill Publishing Co., New York, 1975.
- [31] J. Smagorinsky, General Circulation Experiments with the Primitive Equations, Monthly Weather Review, 91 (1963) 99-164.
- [32] F. Vozzi, F. Bianchi, A. Ahluwalia, C. Domenici, Hydrostatic pressure and shear stress affect endothelin-1 and nitric oxide release by endothelial cells in bioreactors, Biotechnology Journal, 9 (2014) 146-154.
- [33] A.T.D. Le, Computational Fluid Dynamics Modeling of Scalable Stirred Suspension Bioreactors for Pluripotent Stem Cell Expansion, Biomedical Engineering, University of Calgary, Calgary, Alberta, 2016.
- [34] A. Sen, M.S. Kallos, L.A. Behie, Expansion of mammalian neural stem cells in bioreactors: effect of power input and medium viscosity, Brain Res Dev Brain Res, 134 (2002) 103-113. [35] Matplotlib: Python plotting, Matplotlib.org.
- https://matplotlib.org/3.1.1/api/ as gen/matplotlib.pyplot.boxplot.html, 2019 (accessed 24 September 2019).

- [36] M.L. Collignon, A. Delafosse, S. Calvo, C. Martin, A. Marc, D. Toye, E. Olmos, Large-Eddy Simulations of microcarrier exposure to potentially damaging eddies inside minibioreactors, Biochemical Engineering Journal, 108 (2016) 30-43.
- [37] E.T. Papoutsakis, Fluid-Mechanical Damage of Animal-Cells in Bioreactors, Trends in Biotechnology, 9 (1991) 427-437.
- [38] G.I. Taylor, Stability of a viscous liquid contained between two rotating cylinders, Philosophical Transactions of the Royal Society of London Series a-Containing Papers of a Mathematical or Physical Character, 223 (1923) 289-343.